Investigation of positron annihilation-in-flight using a digital coincidence Doppler broadening spectrometer

2012 New J. Phys. 14 035005

(http://iopscience.iop.org/1367-2630/14/3/035005)

New Journal of Physics
The open-access journal for physics

Investigation of positron annihilation-in-flight using a digital coincidence Doppler broadening spectrometer

Jakub Čížek[1], **Marián Vlček and Ivan Procházka**
Faculty of Mathematics and Physics, Charles University in Prague,
V Holešovičkách 2, Prague 8, CZ-18000, Czech Republic
E-mail: jakub.cizek@mff.cuni.cz

New Journal of Physics **14** (2012) 035005 (18pp)
Received 1 November 2011
Published 2 March 2012
Online at http://www.njp.org/
doi:10.1088/1367-2630/14/3/035005

Abstract. This work reports on precise measurements of two-quantum positron annihilation-in-flight using a digital coincidence Doppler broadening spectrometer. Annihilation-in-flight was measured for positrons emitted by ^{68}Ge/^{68}Ga and ^{22}Na radioisotopes and for various targets. Experimental data were compared with theoretical prediction by quantum electrodynamics. It was found that two-quantum positron annihilation-in-flight can be clearly recognized in two-dimensional coincidence Doppler broadening spectra as a hyperbolic curve with shape described well by the relativistic theory. The contribution of annihilation-in-flight is determined predominantly by the energy of incident positrons and is only weakly dependent on the target material. The profile of the positron annihilation-in-flight contribution for positron kinetic energies above 100 keV is well described by theory.

Contents

[1] Author to whom any correspondence should be addressed.

1. Introduction

Coincidence Doppler broadening (CDB) spectroscopy introduced by Lynn *et al* [1] is nowadays frequently used in solid state physics [2–4]. The CDB technique is based on a precise measurement of the energy of two gamma rays emitted simultaneously in the process of positron annihilation using a coincidence apparatus equipped with two high-purity germanium (HPGe) detectors. The energies of the two annihilation gamma rays differ due to the Doppler shift caused by non-zero momentum of the annihilating electron–positron pair in the laboratory frame. An energetic positron implanted in a solid loses most of its kinetic energy within ∼0.1 ps in collisions with electrons [5] and reaches thermal equilibrium with the host material typically within a few ps [6]. Since the contribution of the thermalized positron to the momentum of the annihilating pair is negligible, the Doppler shift in the energy of the annihilation gamma rays can be directly correlated to the electron momentum. Most positrons are annihilated in the thermalized state. However, there is a small but non-zero probability that the positron is annihilated prior to its thermalization, i.e. during the slowing down process. In such rare events, called annihilation-in-flight, the Doppler shift is determined predominantly by the positron momentum, which substantially exceeds the momentum of the electron.

Two-quantum annihilation-in-flight (TQAF) has been observed in the past by several authors. The TQAF process for positrons with energies from ∼1 to 200 MeV was measured in early works [7, 8] using beta and gamma scintillation counters. The total TQAF cross sections for positron energies of 0.765, 1.02, 2.2 and 3.33 MeV in the anthracene target were determined by Kendall and Deutsch [8] and were found to be in good agreement with theoretical predictions given by quantum electrodynamics (QED) [9]. The interest in TQAF was revived due to the search for anomalies in the electron–positron scattering cross section near the Z^0 mass [10, 11] and the search for new particles carried out using positron annihilation-in-flight [12, 13]. More recently a signature of TQAF was observed in a two-dimensional (2D) energy spectra measured on a coincidence apparatus consisting of two HPGe detectors [14–16]. CDB spectroscopy enables us to measure the TQAF process simultaneously for positrons with various energies. However, because of very low statistics and difficulties in discerning the TQAF contribution from the random background, no attempt to determine the TQAF cross section from CDB spectra has been made so far. There is also a lack of a systematic study of TQAF in various targets.

Recently we developed a new digital CDB spectrometer [17] where pulses from HPGe detectors are sampled in *real time* by a two-channel 12-bit digitizer. The acquired waveforms are stored in a computer and analyzed *off-line* by software. Digital processing enables a detailed examination of the shape of detector signals, and waveforms with distorted shape can be very efficiently eliminated. It has been demonstrated [17] that such a procedure leads to a strong suppression of background in the CDB spectrum. Since TQAF is a very rare process low background is crucial for an accurate measurement of this phenomenon.

In this work, a digital CDB spectrometer was used for low-background TQAF measurement. Systematic investigations of the TQAF process in various targets from low-Z materials (polymers) up to high-Z materials (lead) were performed. In long-term CDB measurements, we accumulated high statistics sufficient for the determination of the TQAF cross section for positron energies from 0.1 up to 1.3 MeV. The TQAF cross sections obtained in experiment were compared with QED theoretical prediction.

2. Experimental details

The measurements reported in this work were made using a digital CDB spectrometer described in [17]. The spectrometer is equipped with two HPGe detectors Canberra GC3519 and GC3018. We used the so-called 'semi-digital' configuration shown schematically in figure 1. The source–sample sandwich is positioned symmetrically between two HPGe detectors at the distance r from both detectors and at the distance d from the common axis of detectors. Unless explicitly stated otherwise, the distance d was zero. The pulses from HPGe detectors are first amplified and sharpened using a semi-Gaussian filter (time constant 4 μs) in spectroscopy amplifiers Canberra 2020 in order to improve the signal-to-noise ratio. Shaped pulses are sampled in real time by a two-channel 12-bit digitizer Acqiris DC 440 (Agilent Technologies). The digitizer is externally triggered by a timing circuit ensuring that only such events when two photons were detected simultaneously in both detectors are accepted. Each acquired waveform consists of 1000 points taken with the sampling period of 20 ns. Analysis of sampled waveforms is performed *off-line* by software using the algorithm described in detail in [17]. The analysis is performed in two steps:

(i) the amplitude of each waveform is determined by parabolic fitting and the energy spectrum of detected gamma rays is constructed for each detector. In this step, a raw selection of waveforms is performed using the so-called *fixed filters* rejecting seriously distorted signals. Fixed filters described in detail in [17] are watchdogs which reject waveforms having some of the following deficiencies: (a) the amplitude of the pulse falls outside the vertical range of the digitizer, (b) baseline prior to the pulse exhibits too high rms, (c) parabolic fitting of the pulse amplitude performed in the range covering 40 channels around the raw pulse maximum (channel with the highest number of counts) gave too high χ^2 values, i.e. refinement of the pulse maximum position failed. Subsequently, each waveform is normalized to the same amplitude and shifted in the time scale to set the position of its maximum to a common reference time corresponding to the channel where most waveforms reached their maximum. Note that due to external triggering by a uniform logical signal produced in timing circuit, for most waveforms the maximum is reached at very similar positions. A waveform is accepted only if its maximum occurs in the time window of $\pm$2000 ns around the reference point, i.e. if the required horizontal shift of the waveform is not higher than 100 points. An ideal waveform shape is constructed from the normalized waveforms using the most frequent value for each time point. As an example, the ideal waveform shape for the detector Canberra GC3519 is shown in figure 2.

(ii) Fine selection of waveforms is performed by the application of *shape filters*. The shape of each normalized waveform is compared with the ideal shape determined in the step (i). A waveform is accepted only if it everywhere falls within a certain band around the ideal shape. Lower and upper limits of this band are set independently for each channel at positions where the distribution created from normalized waveforms in this channel falls to 1/10 of its maxima.

In the following text the spectrum constructed in step (i) from all waveforms which passed raw selection by fixed filters will be called the *raw spectrum* to distinguish it from the *filtered spectrum* constructed in step (ii) only from waveforms accepted by shape filters.

In this work we report the results obtained using two β^+ emitters (i) ^{22}Na (activity $\approx$ 1 MBq), which is the most common source in positron annihilation spectroscopy and

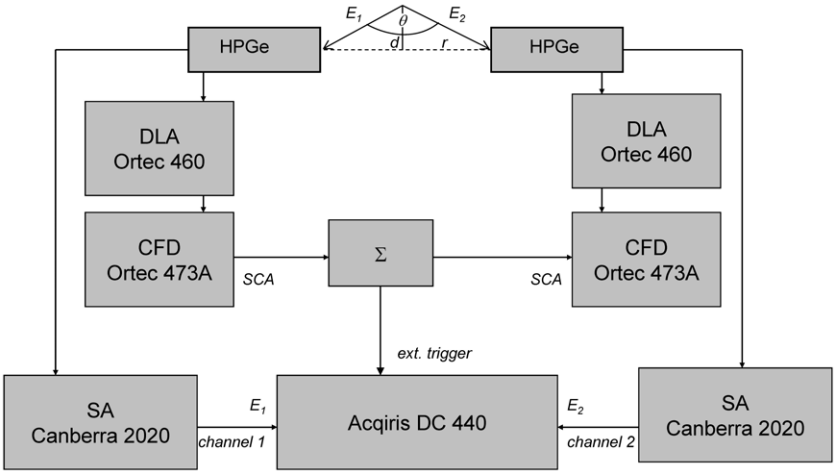

Figure 1. Scheme of the digital CDB spectrometer that was used in this work. HPGe, high-purity Ge detector; DLA, delay line amplifier; CFD, constant fraction dicriminator; Σ, impedance matched passive summing circuit; SA, spectroscopy amplifier.

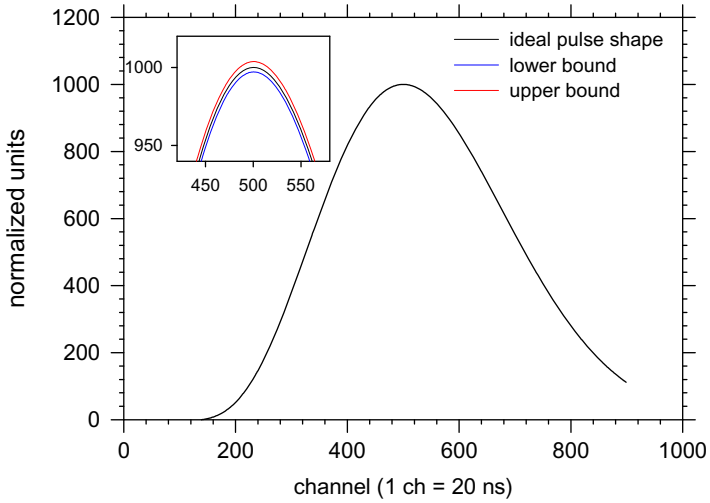

Figure 2. The ideal shape of the waveform for the HPGe detector Canberra GC3519. The inset shows a zoomed detail around the maximum with the lower and upper bounds. Note that the first 100 and last 100 channels are not used because these channels may not be available due to the horizontal shift of the waveform to a common reference position.

(ii) ^{68}Ge/^{68}Ga (activity ≈ 0.6 MBq). Positrons emitted by ^{22}Na exhibit a continuous energy spectrum with the end-point energy $T_{+,f} = 545$ keV. One secondary gamma quantum with an energy of 1274 keV is emitted per each positron due to de-excitation of the daughter ^{22}Ne nucleus. The ^{68}Ge/^{68}Ga positron generator is more suitable for the investigation of the TQAF process because of the higher end-point energy of emitted positrons ($T_{+,f} = 1897$ keV) and low probability (0.039 per positron) of a secondary gamma ray emission. TQAF was measured

in pure metal targets: Mg, Al, Cu and Pb, and in polymer targets: polytetrafluoroethylene (PTFE) and polystyrene (PS). The total statistics accumulated in CDB spectra was in the range of 10^8–10^9.

3. Theory

Let us consider a TQAF process where a positron with total energy E_+ and momentum $\boldsymbol{p}_+$ is annihilated by the electron at rest with the emission of two gamma quanta with energy E_1 and E_2. From the energy conservation law, it follows that

$$E_+ + m_0c^2 = E_1 + E_2, \tag{1}$$

where m_0 is the electron rest mass and c is the velocity of light. Note that the electron binding energy in matter was omitted in equation (1) because it is negligible compared to the energy of the non-thermalized positron. The conservation of momentum can be expressed as

$$p_+^2c^2 = E_1^2 + E_2^2 + 2E_1E_2\cos\theta, \tag{2}$$

where θ is the angle between the emitted gamma rays; see figure 1. Combining equations (1) and (2) and using the well-known equation $E_+^2 = m_0^2c^4 + p^2c^2$, one obtains a relation that bounds energies E_1, E_2 of annihilation gamma rays with the angle θ between them

$$\frac{1}{E_1} + \frac{1}{E_2} = \frac{1-\cos\theta}{m_0c^2}. \tag{3}$$

2D CDB spectra of annihilation radiation are usually represented by a plot of the sum of detected annihilation gamma ray energies $E_1 + E_2$ versus the difference of these energies $E_1 - E_2$. Hence, for comparison with experiment, it is more convenient to rewrite equation (3) in the form

$$E_1 + E_2 = \sqrt{(E_1 - E_2)^2 + \left(\frac{2m_0c^2}{1-\cos\theta}\right)^2} + \frac{2m_0c^2}{1-\cos\theta}, \tag{4}$$

which relates the sum $E_1 + E_2$ with the difference $E_1 - E_2$ and the angle θ. In the CDB spectrometer, HPGe detectors are oriented face-to-face, see figure 1. This configuration limits the TQAF contribution to the CDB spectrum only to events with constant angle θ determined by the distance d of the positron source from the common axis of detectors. The curve described by equation (4) is plotted in figure 3 for various angles θ. For a fixed angle θ the TQAF contribution to the CDB spectrum has a hyperbolic shape with the minimum occurring at $E_1 - E_2 = 0$. The vertical position of the minimum is located at

$$(E_1 + E_2)_{\min} = \frac{4m_0c^2}{1-\cos\theta}, \tag{5}$$

i.e. for $\theta = 180^\circ$ the minimum is located at $(E_1 + E_2)_{\min} = 2m_0c^2$. With decreasing angle θ, the TQAF hyperbola is gradually shifted up, i.e. to higher energies. The minimum angle $\theta_{\min}$ between annihilation gamma rays is determined by the end-point kinetic energy of emitted positrons $T_{+,f}$. Obviously, $E_1 + E_2$ cannot be higher than $T_{+,f} + 2m_0c^2$, which implies that the minimum angle between the annihilation gamma rays is given by the relation

$$(\cos\theta)_{\min} = \frac{T_{+,f} - 2m_0c^2}{T_{+,f} + 2m_0c^2}. \tag{6}$$

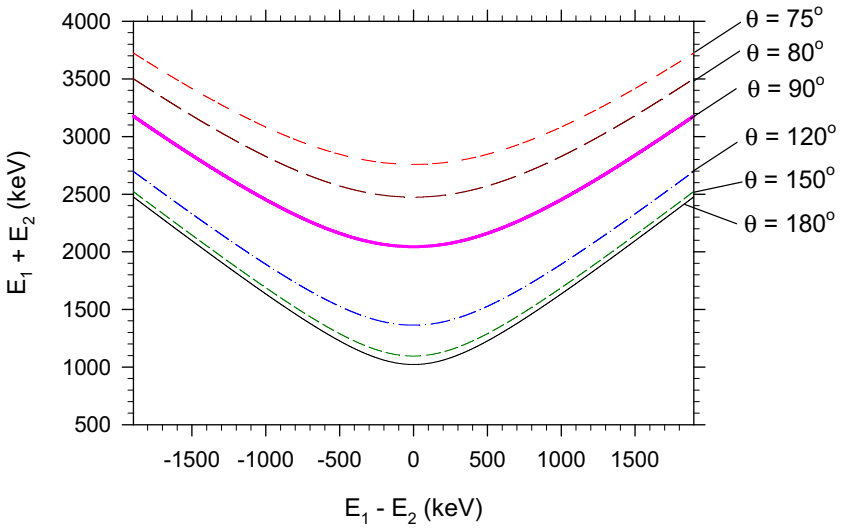

Figure 3. TQAF contribution to the CDB spectrum calculated using equation (4) for various angles θ.

In the case of a ^{22}Na radioisotope emitting positrons with the end-point energy $T_{+,f} = 545\,\text{keV}$, the angle between annihilation gamma rays cannot be smaller than $\theta_{\min} = 107.7^\circ$, while for ^{68}Ge/^{68}Ga, which produces positrons with $T_{+,f} = 1897\,\text{keV}$, the minimum angle between the annihilation gamma rays becomes $\theta_{\min} = 72.5^\circ$.

The TQAF cross section Φ_{TQAF} per electron for the annihilation of a positron with total energy E_+ and an electron at rest was calculated by Dirac [18]:

$$\Phi_{\text{TQAF}} = \pi r_0^2 \frac{1}{\gamma+1}\left[\frac{\gamma^2+4\gamma+1}{\gamma^2-1}\ln\left(\gamma+\sqrt{\gamma^2-1}\right) - \frac{\gamma+3}{\sqrt{\gamma^2-1}}\right], \tag{7}$$

where r_0 is the classical electron radius and γ is the total positron energy expressed in units of the electron rest mass $\gamma = E_+/m_0c^2$.

The probability that a positron will be annihilated by the TQAF process during slowing down from kinetic energy $T_+ + \mathrm{d}T_+$ to T_+ in a target having density ρ and atomic number Z can be expressed as

$$p(T_+) = -\frac{N_{\text{A}}\rho Z}{A}\frac{\Phi_{\text{TQAF}}(T_+ + m_0c^2)}{S(T_+ + m_0c^2)}\,\mathrm{d}T_+, \tag{8}$$

where N_A is Avogadro's number and A is the atomic weight of the absorber. The positron stopping power $S(E_+)$ was calculated in [19] taking into account energy losses in inelastic and elastic collisions and by bremsstrahlung radiation. The positron stopping power can be represented by a product of two functions which depend on the total energy of the positron (expressed in units of the rest electron mass) and the atomic number Z of the absorbing material:

$$S(E_+) = \frac{\mathrm{d}E_+}{\mathrm{d}x} = -\rho(a_1 Z + a_2)\frac{\gamma^{2.4}}{\gamma^{1.9}-1}, \tag{9}$$

where a_1 and a_2 are material constants characterizing the absorber. For targets with $Z \leqslant 38$, $a_1 = -5.95\,\text{g}^{-1}\,\text{cm}^2\,\text{keV}$, $a_2 = 928\,\text{g}^{-1}\,\text{cm}^2\,\text{keV}$, while for targets with $Z > 38$, $a_1 = -2.85\,\text{g}^{-1}\,\text{cm}^2\,\text{keV}$, $a_2 = 810\,\text{g}^{-1}\,\text{cm}^2\,\text{keV}$ [19].

From equation (8), it follows that the TQAF probability for a positron with *constant* energy is proportional to the electron density in the target. However, equation (9) shows that in materials with a higher electron density, the positron loses its energy *faster*. These two effects partially cancel each other and the total TQAF probability for positrons emitted by a radioisotope with the end-point energy $T_{+,f}$ is given by the expression

$$P(T_+) = \frac{N_A}{A}\frac{Z}{a_1 Z + a_2}\int_{T_+}^{T_{+,f}} \mathrm{d}T_+ q(T_+, T_{+,f})\,\Phi_{\mathrm{TQAF}}\left(T_+ + m_0c^2\right)\sqrt{m_0c^2}\frac{\left(T_+ + m_0c^2\right)^{1.9} - \left(m_0c^2\right)^{1.9}}{\left(T_+ + m_0c^2\right)^{2.4}}. \tag{10}$$

Here, the function $q(T_+, T_{+,f})$ denotes the energy distribution of positrons emitted by a β^+ radioisotope [20, 21]

$$q\left(T_+, T_{+,f}\right) = D\sqrt{T_+\left(T_+ + 2m_0c^2\right)}\left(T_+ + m_0c^2\right)\left(T_{+,f} - T_+\right)^2, \tag{11}$$

where D is a normalization coefficient.

Hence, $P(T_+)$ is independent of ρ and is only weakly dependent on Z, since the factor $Z/A(a_1Z + a_2)$ varies only very slightly for various materials. This implies that the TQAF probability $P(T_+)$ is determined mainly by the energy of incident positrons and is almost independent of the target material.

4. Results and discussion

Figure 4 shows a 2D CDB spectrum, i.e. the sum of the energies of detected gamma rays $E_1 + E_2$ plotted against the difference of these energies $E_1 - E_2$ for positrons emitted by a ^{68}Ge/^{68}Ga radioisotope into the Mg target ($d = 0$). Figure 4(a) shows the raw spectrum obtained in step (i) of data analysis, i.e. the spectrum constructed from all waveforms that passed raw selection by fixed filters. The filtered CDB spectrum constructed only from waveforms that were accepted by digital shape filters is plotted in figure 4(b). The vertical cut at $E_1 - E_2 = 0$ and the horizontal cut at $E_1 + E_2 = 2m_0c^2$ from the 2D CDB spectra are plotted in figures 5(a) and (b), respectively. The main contribution to CDB spectra comes from the annihilation of thermalized positrons, which is represented by a strong peak located at $E_1 + E_2 = 2m_0c^2$ and $E_1 - E_2 = 0$. All CDB spectra in this paper were normalized to the same maximum of this peak. An additional peak that is located at $E_1 + E_2 = 4m_0c^2$ and $E_1 - E_2 = 0$ (see figure 5(a)) represents 'four-photon' events where two independent annihilations of the thermalized positron occur in a time interval so short that they are considered to be a single event. Since two annihilation photons were detected in each detector, the sum of energy deposited in the detectors is four times the rest electron mass. The maximum of a waveform formed by a superposition of pulses from two independent annihilations corresponds to the energy of $2m_0c^2$ only when both events occur almost simultaneously, i.e. within a very short time interval compared to the pulse duration. Waveforms formed by random summation of annihilation events which appeared within a longer time interval exhibit a maximum that is lower since pulses from these two annihilation events are shifted in time with respect to each other. As a consequence the peak at $E_1 + E_2 = 4m_0c^2$ is preceded by a slowly decaying tail; see figure 5(a). Since this contribution comes from the annihilation of thermalized positrons the difference of gamma ray energies is very small and the contribution appears in 2D CDB spectra in figure 4(a) as a vertical line. An abrupt drop of this tail that can be observed at $E_1 + E_2 \approx 1850$ keV occurs when the time distance between two

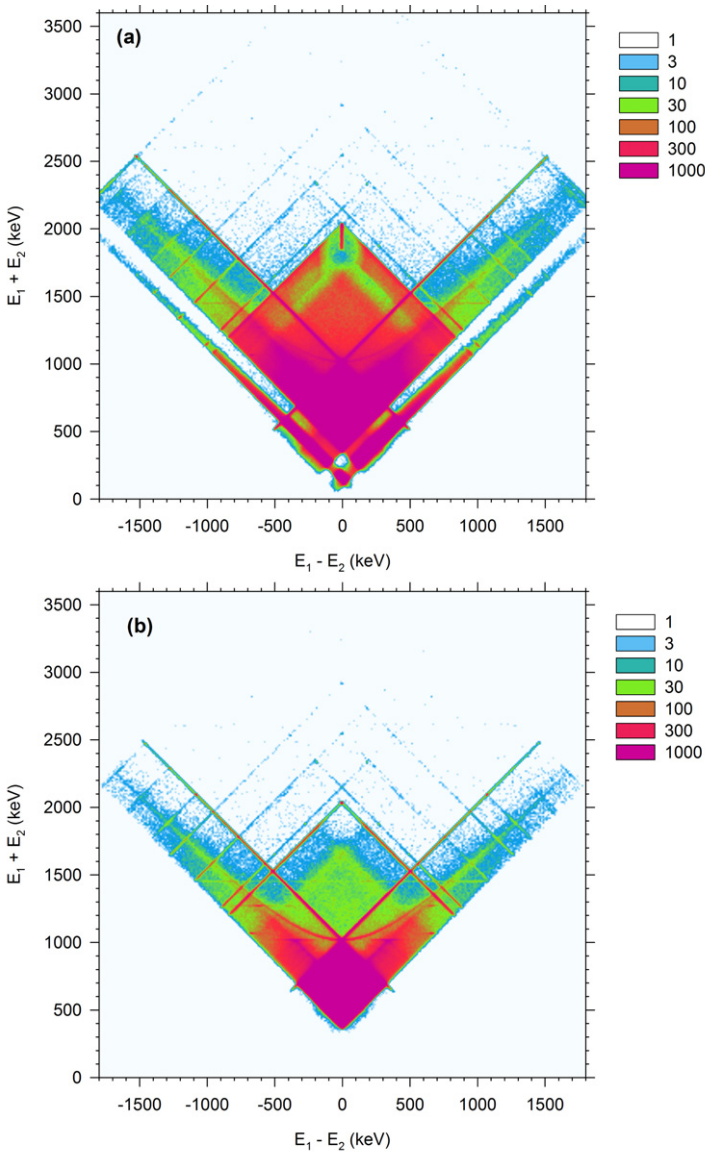

Figure 4. 2D CDB spectra measured in the Mg target using positrons emitted by ^{68}Ge/^{68}Ga radioisotopes, $d = 0$. (a) Raw spectrum constructed from all waveforms which passed raw selection by fixed filters. (b) Filtered spectrum constructed only from waveforms accepted by shape filters. Counts are color coded from 1 to 1000 and larger per bin on the log10 scale. To enhance the features caused by rare events, all bins with more than 1000 counts were set to 1000.

annihilation events becomes so large that a horizontal shift of the maximum of the superimposed waveform exceeds 100 channels (2000 ns) and such events are rejected by fixed filters already in step (i) of the analysis.

Figure 5(a) demonstrates that the application of shape filters leads to a significant reduction of background above the main peak at $E_1 + E_2 = 2m_0c^2$ due to the rejection of pulses with shape distorted by random summation with another event. Moreover, the tail preceding the

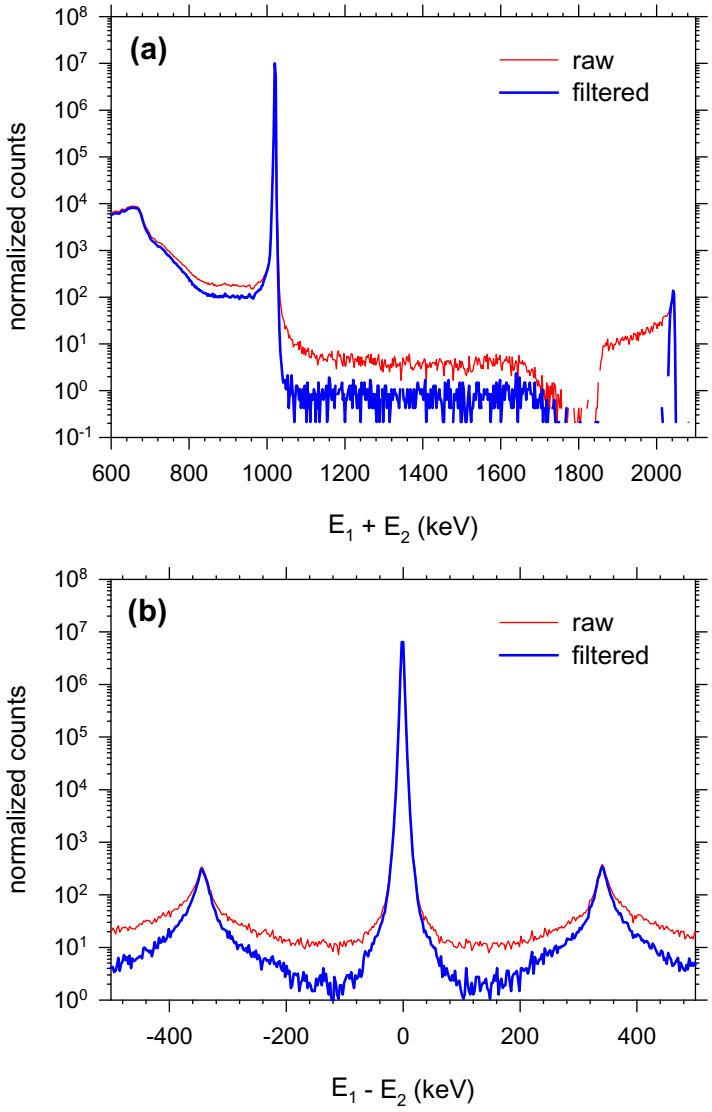

Figure 5. (a) Vertical cuts at E_1–$E_2 = 0$ and (b) horizontal cuts at $E_1 + E_2 = 2m_0c^2$ from the 2D CDB spectra from figure 4. Thin lines represent cuts from the raw spectrum in figure 4(a). Thick lines show cuts from the filtered CDB spectrum in figure 4(b) constructed only from waveforms accepted by shape filters.

'four-photon' peak at $E_1 + E_2 = 4m_0c^2$ was completely removed by the application of shape filters.

The number of annihilation events contributing to the main annihilation peak at $E_1 + E_2 = 2m_0c^2$ is given by the expression

$$N_{2\gamma} = A\beta \frac{S_{\text{det}}}{4\pi r^2} P_{2\gamma} \eta_1 \eta_2 t, \tag{12}$$

where A is the activity of the positron source, β is the branching ratio for the β^+ decay ($\beta = 0.89$ for ^{68}Ge/^{68}Ga), S_{det} is the active area of the detector and r is the distance between the source and the detector; see figure 1. In our setup, S_{det} and r are the same for both detectors. The symbol

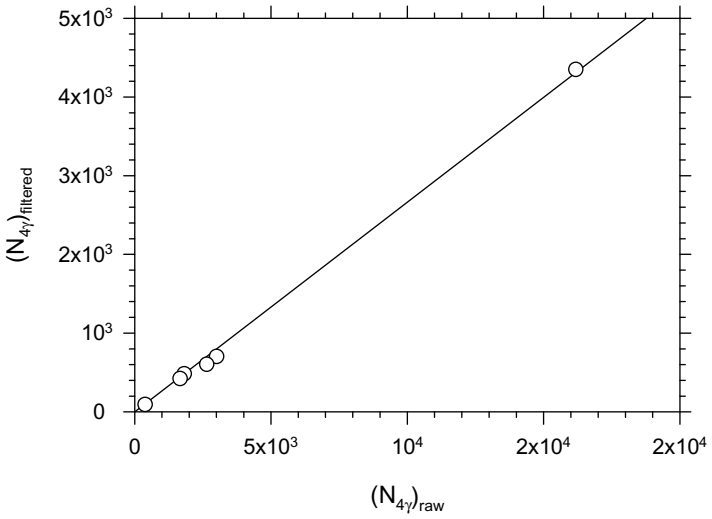

Figure 6. Relation between the area of the 'four-photon' peak in filtered and raw CDB spectra. The area $(N_{4\gamma})_{\text{filtered}}$ of the 'four-photon' peak in the filtered spectrum is plotted against the area $(N_{4\gamma})_{\text{raw}}$ of the 'four-photon' peak in the raw spectrum.

$P_{2\gamma}$ denotes the probability that the positron is annihilated in the thermalized state, η_1 and η_2 stand for the absolute efficiency of detectors for annihilation gamma rays and t is the total time of measurement. The number of annihilation events contributing to the 'four-photon' peak at $E_1 + E_2 = 4m_0c^2$ can be obtained from the equation

$$N_{4\gamma} = \left(A\beta \frac{S_{\text{det}}}{4\pi r^2} P_{2\gamma}\eta_1\eta_2 \right)^2 \tau t, \tag{13}$$

where τ is the time interval between waveforms for which they are considered as a single event. The ratio between the area of the 'four-photon' peak and the main annihilation peak

$$\frac{N_{4\gamma}}{N_{2\gamma}} = A\beta \frac{S_{\text{det}}}{4\pi r^2} P_{2\gamma}\eta_1\eta_2\tau \tag{14}$$

enables us to estimate the time interval τ. For the spectrum shown in figure 5(a), we obtained $N_{4\gamma}/N_{2\gamma} \approx 2.5 \times 10^{-5}$. Using the known activity of the positron source $A \approx 0.6$ MBq, the active area of detectors $S_{\text{det}} \approx 25\,\text{cm}^2$, the distance of detectors from the source $r \approx 27$ cm, the measured absolute efficiency of detectors for 511 keV gamma rays $\eta_1 \approx 0.09$, $\eta_2 \approx 0.10$ and $P_{2\gamma} \approx 0.98$ [16], we obtained $\tau \approx 1940$ ns, which agrees with the upper limit of 100 channels (1 channel = 2000 ns) imposed on the horizontal shift of a waveform by software in step (i) of the analysis.

The ratio of the area of the 'four-photon' contribution $(N_{4\gamma})_{\text{filtered}}$ in the filtered spectrum to the area $(N_{4\gamma})_{\text{raw}}$ in the raw spectrum is equal to the ratio of time intervals for which the pulses are considered as a single event

$$\frac{(N_{4\gamma})_{\text{filtered}}}{(N_{4\gamma})_{\text{raw}}} = \frac{\tau_{\text{filtered}}}{\tau_{\text{raw}}}. \tag{15}$$

Figure 6 shows $(N_{4\gamma})_{\text{filtered}}$ plotted against $(N_{4\gamma})_{\text{raw}}$ for spectra measured in the same geometry using ^{22}Na and ^{68}Ge/^{68}Ga sources with various activities. Obviously, the data in

figure 6 agree well with equation (15) and the ratio of time intervals was found to be $\tau_{\text{filtered}}/\tau_{\text{raw}} \approx 1/4$. Hence, the application of shape filters improves the time resolution power by a factor of 4.

One can see in figure 5(a) that the application of shape filters leads to a background suppression also in the region $E_1 + E_2 < 2m_0c^2$, i.e. prior to the annihilation peak. This is due to the rejection of waveforms with shape distorted by the ballistic deficit. Hence, digital shape filters represent a very efficient way to suppress the undesired background originating mainly from random pile-up events and pulses distorted due to the ballistic deficit.

Figure 5(b) shows horizontal cuts (at $E_1 + E_2 = 2m_0c^2$) of spectra in figure 4. The central peak in figure 5(b) represents the contribution of annihilation of thermalized positrons. The side peaks in figure 5(b) are due to Compton scattering when one annihilation gamma ray is backscattered from one detector to the second detector. Since the backscattered annihilation gamma ray (scattering angle 180°) deposits in one detector an energy of 340.7 keV (the Compton edge) and carries out energy of 170.3 keV, which is deposited in the second detector, the energy difference between the two detectors is $2 \times 170.3 = 340.6$ keV, which corresponds to the maximum of the side peaks in figure 5(b). One can see in figure 5(b) that the application of shape filters leads to a significant reduction of background around the central annihilation peak. However, the side peaks caused by backscattered gamma rays remain unaltered since this is a causal effect that produces pulses of proper shape.

2D CDB spectra in figure 4 exhibit a hyperbolic shape feature representing the contribution of the TQAF process. From figure 4, it is clear that the TQAF contribution is much more visible in figure 4(b), where undesired background was reduced by the application of shape filters. A comparison of the CDB spectrum from figure 4(b) with the theoretical shape of the TQAF contribution is shown in figure 7. It is clear that the shape of the TQAF contribution measured in experiment agrees well with the theoretical shape described by equation (4) with $\theta = 180°$. The width of the TQAF hyperbola is determined by the range of angles θ for which annihilation gamma rays can be registered in detectors. In our setup, in the central geometry (i.e. $d = 0$) gamma rays emitted with angles θ from 180° to 165° can be detected. This corresponds to the width of the TQAF hyperbola of about 18 keV.

Figure 8 shows the filtered 2D CDB spectrum measured using positrons emitted by the ^{68}Ge/^{68}Ga source and implanted in the Mg target. The measurement was made in off-axis geometry with the source–sample sandwich placed at the distance $d = 4$ cm from the common axis of the detectors; see figure 1. In this geometry, TQAF gamma rays with angle $\theta = 163° \pm 15°$ are detected, which leads to a shift of the TQAF hyperbola to higher energies. The TQAF contribution calculated using equation (4) with $\theta = 163°$ is plotted in figure 8 by a solid line. Obviously the calculated curve agrees well with the experimental data. Since, in this experiment, d was larger than the diameter of the detector active area, true coincidences caused by annihilations of thermalized positrons with emission of two anti-collinear gamma rays cannot be detected. As a consequence the central peak located at $E_1 - E_2 = 0$ and $E_1 + E_2 = 2m_0c^2$ becomes significantly smaller because now it is caused only by random coincidences of two independent annihilations of thermalized positrons. Note that a vertical line at the energy $E_1 + E_2 = 1461$ keV, which is clearly visible in figure 8, is due to backscattering of 1461 keV gamma rays emitted from the natural background by a ^{40}K radioisotope (half-life 1.3 billion years) from one detector to the second one.

Figure 9 shows the filtered 2D CDB spectrum measured in the same geometry as the spectra in figure 4, i.e. $d = 0$, but using positrons emitted by a ^{22}Na radioisotope into the Al target.

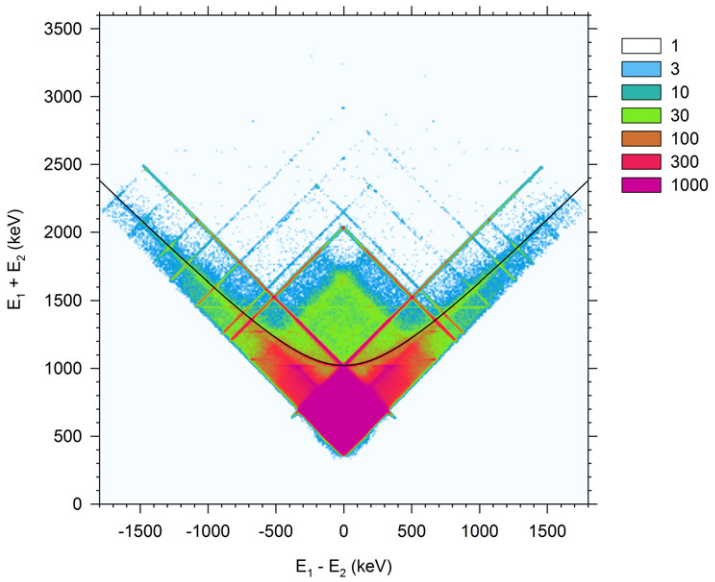

Figure 7. A comparison of the 2D CDB spectrum from figure 4(b) with the theoretical shape of the TQAF contribution calculated by equation (4) with $\theta = 180^\circ$ and plotted in the figure by a solid line. Counts are color coded from 1 to 1000 and larger per bin on a log10 scale. To enhance the features caused by rare events, all bins with more than 1000 counts were set to 1000.

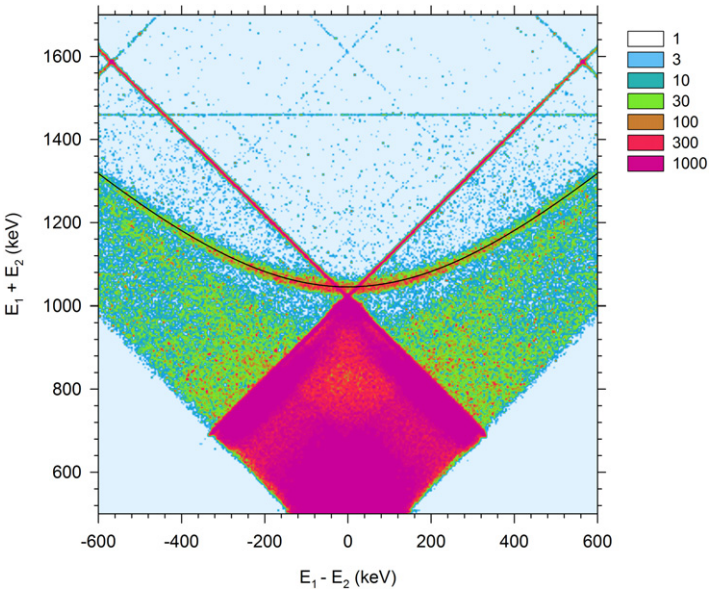

Figure 8. The 2D CDB spectrum measured using the ^{68}Ge/^{68}Ga positron source and the Mg target. The source–sample sandwich was placed off-axis at a distance $d = 4$ cm from the common detector axis. The theoretical shape of the TQAF contribution calculated by equation (4) with $\theta = 163^\circ$ is plotted by a solid line. Counts are color coded from 1 to 1000 and are larger per bin on the log10 scale. To enhance features caused by rare events, all bins with more than 1000 counts were set to 1000.

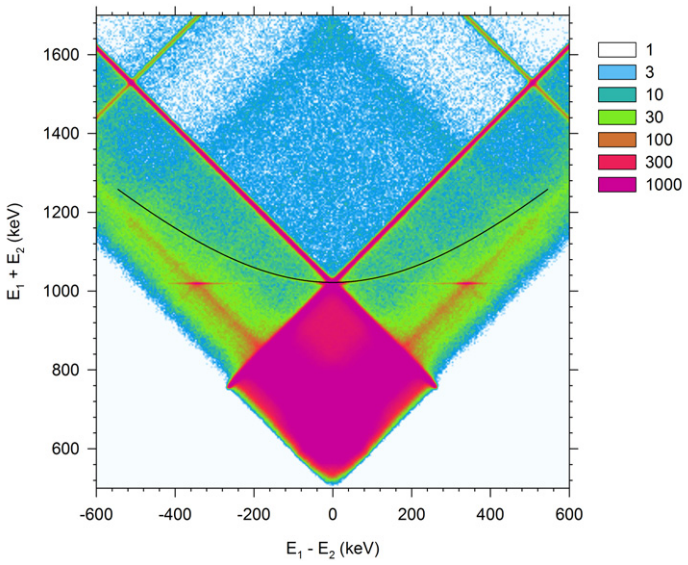

Figure 9. The 2D CDB spectrum measured using the ^{22}Na positron source and the Al target, $d = 0$. The theoretical shape of TQAF contribution calculated using equation (4) with $\theta = 180^\circ$ is plotted by a solid line. Counts are color coded from 1 to 1000 and larger per bin on a log10 scale. To enhance the features caused by rare events, all bins with more than 1000 counts were set to 1000.

The TQAF contribution calculated using equation (4) with $\theta = 180^\circ$ plotted by the solid line agrees well with experimental data. The vertical cut (at $E_1 - E_2 = 0$) and the horizontal cut (at $E_1 + E_2 = 2m_0c^2$) from the spectrum in figure 9 are plotted in figures 10(a) and (b), respectively. Obviously, the cuts from the 2D CDB spectra exhibit features similar to those found previously in the cuts from the spectrum measured using positrons emitted by the ^{68}Ge/^{68}Ga source, cf figure 5. This is not surprising as these features are caused predominantly by gamma rays emitted during annihilation of thermalized positrons.

Figure 11 shows histograms of counts along the TQAF contribution. The histogram in figure 11(a) was obtained from the filtered 2D CDB spectrum in figure 4(b) (the ^{68}Ge/^{68}Ga source and Mg target) as a curved cut along the curve given by equation (4). Figure 11(b) shows the histogram obtained in a similar way from the filtered 2D CDB spectrum in figure 9 (the ^{22}Na source and Al target). A strong peak at $E_1 - E_2 = 0$ is due to annihilation of thermalized positrons. The symmetrical tail on both sides of the peak represents the contribution of the TQAF process. Obviously, due to higher end-point energy of emitted positrons the TQAF tail extends to higher energies in the histogram measured using a ^{68}Ge/^{68}Ga radioisotope (figure 11(a)). Moreover, one can see in figure 11 that the TQAF contribution decreases with increasing the difference in energy of annihilation gamma rays in agreement with decreasing probability for TQAF expressed by equation (10). For a quantitative comparison of experiment with theory, background was subtracted from TQAF experimental profile. Background level was estimated independently for each bin of the histogram in figure 11 as an average of the local background level below and above the TQAF hyperbola. For the determination of the background level below the TQAF hyperbola, we used a band with the same shape as the TQAF contribution but shifted downwards (i.e. to lower $E_1 + E_2$) by 10 keV. Similarly,

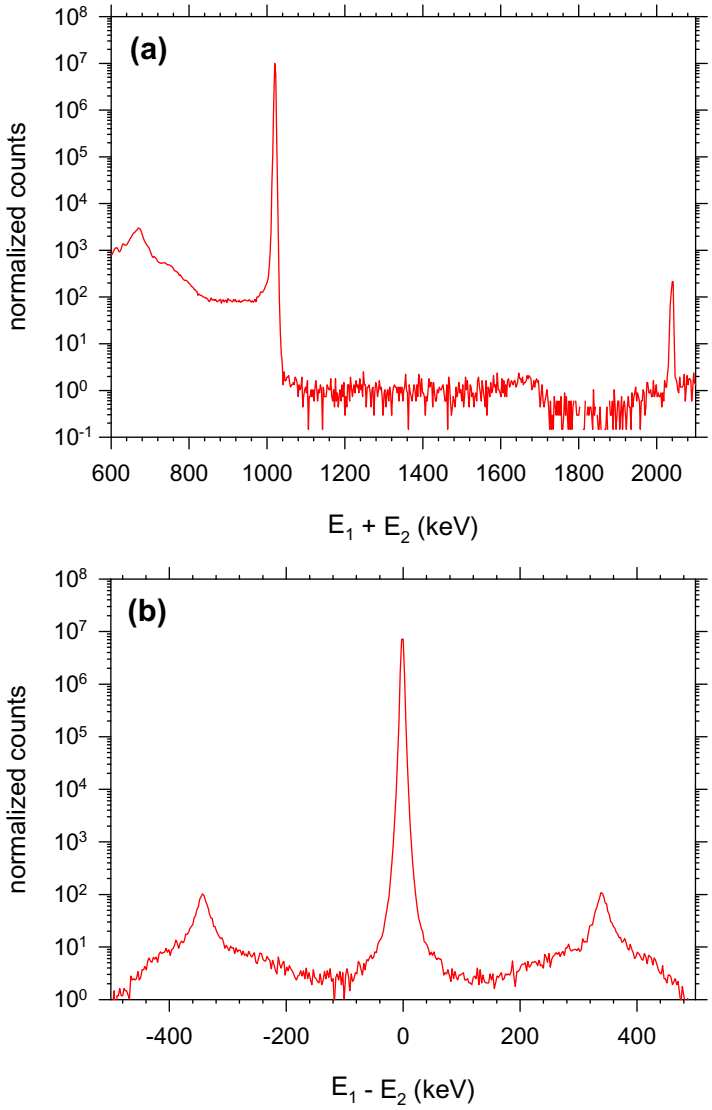

Figure 10. (a) Vertical cuts at E_1–$E_2 = 0$ and (b) horizontal cuts at $E_1 + E_2 = 2m_0c^2$ from the 2D CDB spectrum in figure 9 measured using positrons emitted by the ^{22}Na source and implanted in the Al target.

the background level above the TQAF hyperbola was determined in a band having the shape of the TQAF contribution but shifted up (i.e. to higher $E_1 + E_2$) by 10 keV. The profile of the TQAF contribution with subtracted background is plotted in figure 11 as well. Since the TQAF contribution is symmetrical with respect to the origin at $E_1 - E_2 = 0$, the TQAF profile with subtracted background was folded around the origin and the average of bin content corresponding to the same absolute value of $E_1 - E_2$ was taken. Figure 12 shows the folded TQAF contribution with subtracted background for various targets. The results obtained using positrons emitted by a ^{68}Ge/^{68}Ga radioisotope are plotted in figure 12(a), whereas figure 12(b) shows the results obtained using positrons emitted by ^{22}Na. The x-axis in figure 12 is given in units of positron kinetic energy $T_+ = E_1 + E_2 - 2m_0c^2$. From equation (4) it follows that for TQAF with $\theta = 180^\circ$ the positron kinetic energy T_+ is related to the difference of gamma ray

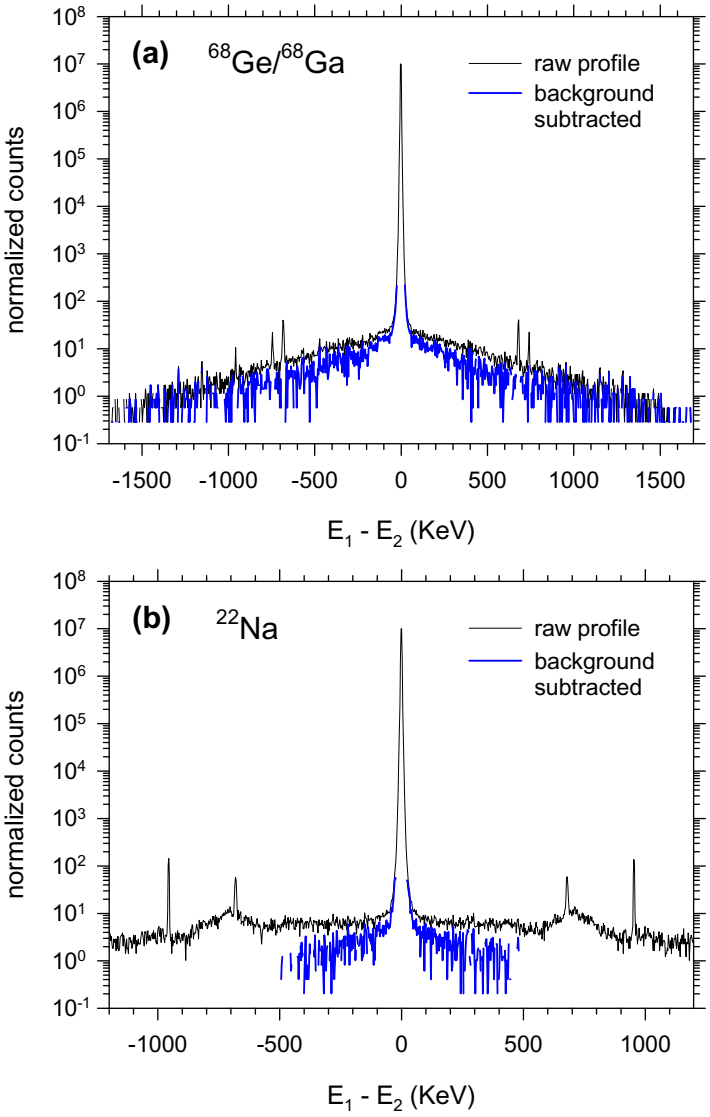

Figure 11. Profile of the TQAF contribution obtained as a curved cut from filtered 2D CDB spectra along the curve given by equation (4) with $\theta = 180^\circ$. The profile with subtracted background is plotted in the figure as well. (a) Results obtained for the ^{68}Ge/^{68}Ga source and the Mg target; (b) the results for the ^{22}Na source and the Al target.

energies $E_1 - E_2$ through the equation

$$T_+ = \sqrt{m_0^2c^4 + (E_1 - E_2)^2} - m_0c^2. \tag{16}$$

From figure 12, it is clear that the profile and intensity of the TQAF contribution for various targets is very similar. Hence, the probability for TQAF is almost independent of the target material in agreement with the prediction given by equation (10). The lines in figure 12 show the TQAF contribution calculated using equation (10) for various targets. Note that the probability for the TQAF process $P(T_+)$ calculated by equation (10) was always multiplied by a constant

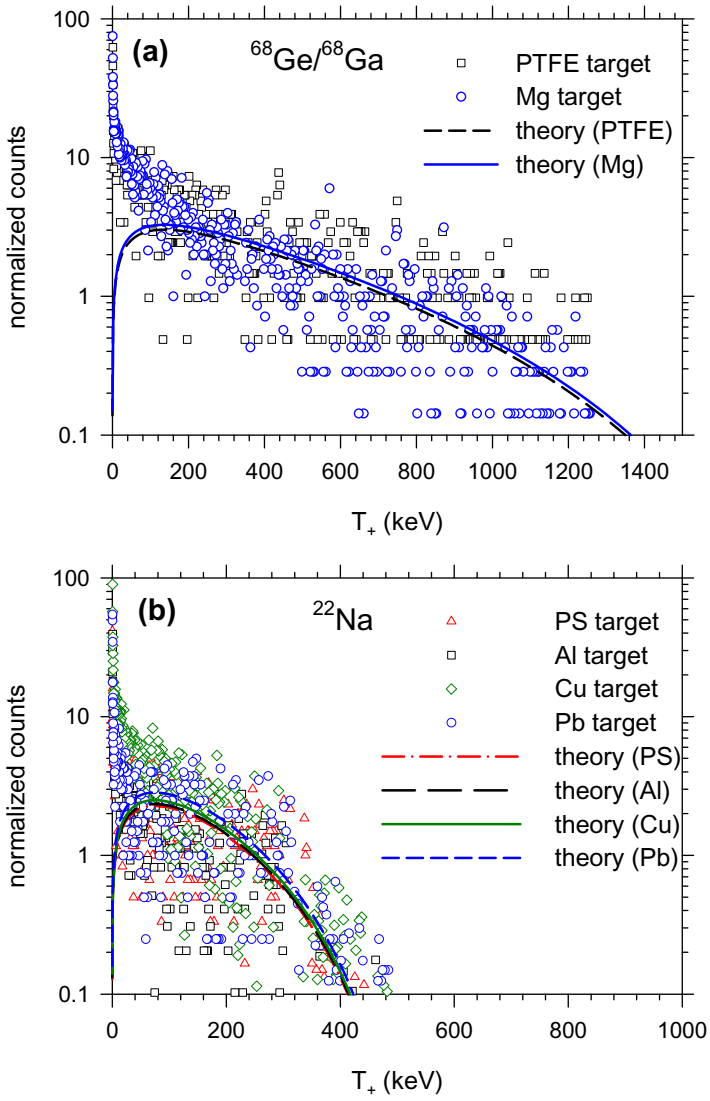

Figure 12. TQAF contributions with subtracted background. Points with the same absolute value of $E_1 - E_2$ corresponding to the same kinetic energy of positron T_+ were averaged. Experimental points are shown for positron energies $T_+ > 10\,\mathrm{keV}$. At lower positron energies it was not possible to distinguish TQAF events from the annihilation of thermalized positrons. Solid lines show theoretical profiles of TQAF contribution calculated using equation (4) with $\theta = 180^\circ$ and multiplied by the constant scaling factor given by equation (17). (a) The results obtained using positrons emitted by ^{68}Ge/^{68}Ga; (b) the results obtained using positrons emitted by the ^{22}Na radioisotope.

scaling factor

$$\xi = A\frac{S_{\mathrm{det}}}{4\pi r^2}\eta_1\eta_2 t. \tag{17}$$

Visual inspection of figure 12 reveals that the experimental points are in reasonable agreement with the theoretical curve for high positron energies $T_+ > 100\,\mathrm{keV}$. This is testified

by the standard χ^2-test, which gave χ^2 values divided by the number of degrees-of-freedom ν falling in the range of 1.06–1.10 for all the targets studied. Since the standard deviation of the χ^2 per degree-of-freedom is $\sigma = (2/\nu)^{1/2} = 0.06$, one can conclude that the experimental data are in satisfactory agreement with theoretical curves for high positron energies $T_+ > 100\,\text{keV}$. At lower positron energies, the experimental points exceed significantly the theoretical prediction for the TQAF contribution. This could be caused by two factors: (i) the contributing annihilation of thermalized positrons and/or (ii) the fact that at low positron energies ($T_+ < 100\,\text{keV}$) equation (9) may become inaccurate and may overestimate the positron-stopping power in the target.

5. Conclusions

In this work, a digital CDB spectrometer was used for the investigation of the TQAF process for positrons emitted by ^{68}Ge/^{68}Ga and ^{22}Na radioisotopes. It was demonstrated that digital processing with the application of shape filters enables us to obtain CDB spectra with very low background. The shape of the TQAF contribution that was clearly resolved in 2D CDB spectra agrees well with the theoretical shape given by the special theory of relativity. It was found that the probability for TQAF is determined predominantly by positron energy and varies only slightly with the target material. The experimental profile of the TQAF contribution agrees well with QED theoretical prediction for positrons with kinetic energy $T_+ > 100\,\text{keV}$.

Acknowledgments

This work was supported by the Czech Science Foundation (project P108/10/0648) and by The Charles University (grant no. SVV-2010-261303).

References

[1] Lynn K G, MacDonald J R, Boie R A, Feldman L C, Gabbe J D, Robbins M F, Bonderup E and Golovchenko J 1977 *Phys. Rev. Lett.* **38** 241
[2] Asoka-Kumar P, Alatalo M, Ghosh V J, Kruseman A C, Nielsen B and Lynn K G 1996 *Phys. Rev. Lett.* **77** 2097
[3] Nagai Y, Hasegawa M, Tang Z, Hempel A, Yubuta K, Shimamura T, Kawazoe Y, Kawai A and Kano F 2000 *Phys. Rev.* B **61** 6574
[4] Somoza A, Petkov M P, Lynn K G and Dupasquier A 2002 *Phys. Rev.* B **65** 094107
[5] Perkins A and Carbotte J P 1970 *Phys. Rev.* B **1** 101
[6] Kubica P and Stewart A T 1975 *Phys. Rev. Lett.* **34** 852
[7] Colgate S A and Gilbert F C 1953 *Phys. Rev.* **89** 790
[8] Kendall H W and Deutsch M 1956 *Phys. Rev.* **101** 20
[9] Heitler W 1954 *The Quantum Theory of Radiation* (Oxford: Oxford University Press)
[10] Adeva B *et al* 1990 *Phys. Lett.* B **250** 199
[11] Akrawy M Z *et al* 1991 *Phys. Lett.* B **257** 531
[12] Fernandez E *et al* 1987 *Phys. Rev.* D **35** 1
[13] Connell S H, Fearick R W, Hoernlé R F A, Sideras-Haddad E and Sellschop J P F 1988 *Phys. Rev. Lett.* **60** 2242
[14] Weber M H, Hunt A W, Golovchenko J A and Lynn K G 1999 *Phys. Rev. Lett.* **83** 4658

[15] Hunt A W, Cassidy D B, Sterne P A, Cowan T E, Howell R H, Lynn K G and Golovchenko J A 2001 *Phys. Rev. Lett.* **86** 5612
[16] Dryzek J, Suyuki T and Runsheng Y 2007 *Radiat. Phys. Chem.* **76** 297
[17] Čížek J, Vlček M and Procházka I 2010 *Nucl. Instrum. Methods* A **623** 982
[18] Dirac P A M 1930 *Proc. Camb. Phil. Soc.* **26** 361
[19] Batra R K and Sehgal M L 1970 *Nucl. Phys.* A **156** 314
[20] Shirokov Yu M and Yudin N P 1980 *Yadernaya Fizika* (Moscow: Nauka)
[21] Krane K S 1987 *Introductory Nuclear Physics* (New York: Wiley)